

PAPER • OPEN ACCESS

## Water driven phase transitions in Prussian white cathode materials

To cite this article: Ida Nielsen *et al* 2022 *J. Phys. Energy* **4** 044012

View the [article online](#) for updates and enhancements.

### You may also like

- [CuS/Prussian blue core-shell nanohybrid as an electrochemical sensor for ascorbic acid detection](#)  
Lihuang Li, Peng Zhang, Ziyang Li et al.
- [The Effect of Insertion Species on Nanostructured Open Framework Hexacyanoferrate Battery Electrodes](#)  
Colin D. Wessells, Sandeep V. Peddada, Matthew T. McDowell et al.
- [Investigations of an organic-inorganic nanotheranostic hybrid for pancreatic cancer therapy using cancer-in-a-dish and in vivo models](#)  
Karolyn Infanta David, T S Ravikumar, Swaminathan Sethuraman et al.



## PAPER

## Water driven phase transitions in Prussian white cathode materials

## OPEN ACCESS

RECEIVED  
9 August 2022REVISED  
28 September 2022ACCEPTED FOR PUBLICATION  
6 October 2022PUBLISHED  
27 October 2022

Original content from  
this work may be used  
under the terms of the  
[Creative Commons  
Attribution 4.0 licence](#).

Any further distribution  
of this work must  
maintain attribution to  
the author(s) and the title  
of the work, journal  
citation and DOI.

Ida Nielsen<sup>1,\*</sup> , Dj Dzodan<sup>1</sup>, D O Ojwang<sup>1</sup> , P F Henry<sup>1,2</sup> , A Ulander<sup>1</sup>, G Ek<sup>1</sup> , L Häggström<sup>1</sup>,  
T Ericsson<sup>1</sup>, H L B Boström<sup>3</sup> and W R Brant<sup>1,\*</sup> <sup>1</sup> Department of Chemistry—Ångström Laboratory, Uppsala University, PO Box 538, SE-75121 Uppsala, Sweden<sup>2</sup> ISIS Pulsed Neutron and Muon Source, Rutherford Appleton Laboratory, Didcot OX11 0QX, United Kingdom<sup>3</sup> Max Planck Institute for Solid State Research, Heisenbergstrasse 1, 70569 Stuttgart, Germany

\* Authors to whom any correspondence should be addressed.

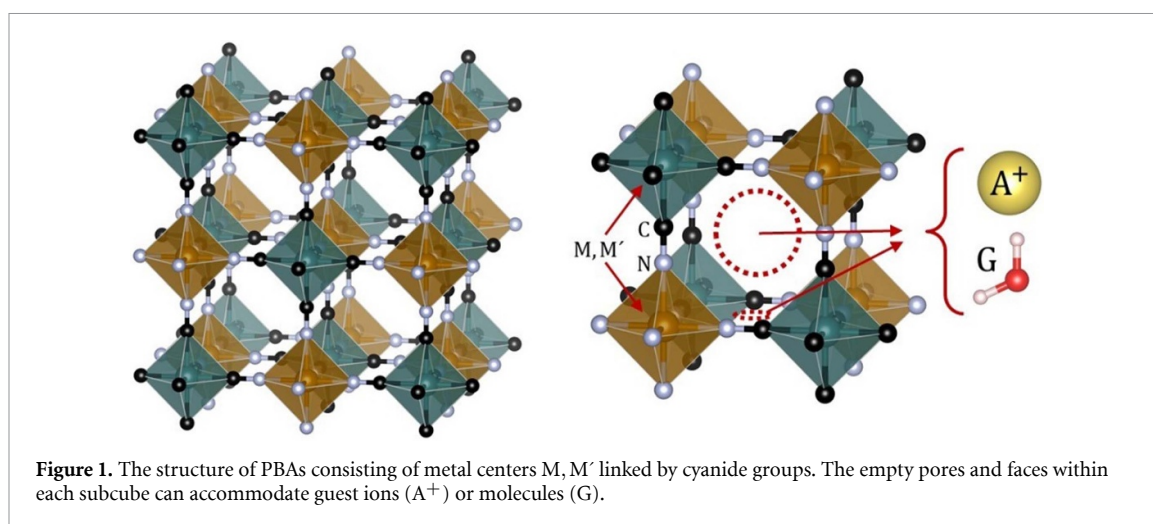
E-mail: [ida.nielsen@kemi.uu.se](mailto:ida.nielsen@kemi.uu.se) and [william.brant@kemi.uu.se](mailto:william.brant@kemi.uu.se)**Keywords:** Prussian blue analogues, sodium-ion batteries, neutron diffraction, sodium iron hexacyanoferrate, octahedral tiltingSupplementary material for this article is available [online](#)**Abstract**

Prussian white (PW,  $\text{Na}_2\text{Fe}[\text{Fe}(\text{CN})_6] \cdot z\text{H}_2\text{O}$ ) is a promising cathode material for use in sodium-ion batteries for large-scale energy storage applications, which demand long cycling life-times. However, for non-aqueous battery applications PW must not contain any water, and yet dehydration induces a large volume change destabilizing the structure and reducing the cycling life. The material undergoes multiple phase transitions as a function of both the sodium and water content, however, the mechanism behind is poorly understood. Here, we use neutron diffraction to explore the influence of water on the structure of PW. For the first time, two structures for a single composition of PW were observed near room temperature independent of the synthesis method. These structures differ in the  $\text{FeN}_6$  and  $\text{FeC}_6$  octahedral tilting configurations, which is connected to the ordering of water in the framework. The removal of water modulates the magnitude of pre-existing structural distortions, if it is itself disordered within the structure, rather than modifying the nature of the distortions. These results provide a robust fundamental understanding of the chemical driving force impacting the nature and magnitude of structural distortions in Prussian blue analogues. The insights provide guidance for designing tilt-engineering ultimately enabling new materials with enhanced long-term electrochemical performance in battery applications.

**1. Introduction**

Prussian blue analogues (PBAs),  $\text{A}_x\text{M}[\text{M}'(\text{CN})_6]_{1-y} \cdot z\text{G}$ , are interesting cathode materials for use in sodium-ion batteries (SIBs) due to their low cost, environmental friendliness, and electrochemical performance [1–3]. The PBA crystal structure can be described as a double perovskite structure consisting of a porous framework with corner-sharing octahedrally coordinated transition metal centers (M, M') linked by cyanide groups (figure 1). The porous framework allows for the inclusion of alkali cations (A) or neutral guest species (G). Further, the compositional flexibility of the framework allows for  $[\text{M}'(\text{CN})_6]^{n-}$  vacancies ( $y$ ). A promising cathode material is the Fe-based,  $[\text{Fe}(\text{CN})_6]^{4-}$  vacancy-free and Na-rich PBA known as Prussian white (PW),  $\text{Na}_2\text{Fe}[\text{Fe}(\text{CN})_6] \cdot z\text{H}_2\text{O}$ , which has an average operating voltage of  $\sim 3.2$  V and a theoretical capacity of  $\sim 170$   $\text{mAhg}^{-1}$  [3, 4].

A major challenge for using PW as a cathode material is its strong affinity to water. That is, the rapid uptake of moisture from the air to be incorporated in the bulk structure as crystal water. The crystal water can be released during charging (sodium removal) reacting with the electrolyte leading to unwanted side reactions in non-aqueous batteries. Further, water oxidizes at high potential leading to irreversible gas formation [5]. The water can be removed through drying, however, this induces an 18% volume contraction which leads to strain and particle cracking [6]. Furthermore, in the absence of water, the structure of PW changes between rhombohedral  $R\bar{3}$  and cubic  $Fm\bar{3}m$  symmetries during electrochemical cycling. This is accompanied by large volume changes,  $\pm 17\%$ , and is responsible for poor cycling stability and loss of



capacity over time [6, 7]. Herein lies the contrary impact of water on the electrochemical performance of PBAs. The presence of water prevents the dramatic volume changes during sodium extraction and insertion, thereby improving structural stability, reducing particle cracking and strain. If such a modification could be maintained over multiple cycles, resistance build up and capacity fade can be reduced. Understanding the origins of phase transitions in PW (and PBAs in general) could allow for chemical modifications to be designed, which suppress the phase transition without the need for water. A recent meta-study of the literature revealed that distortions in PBAs in general occur when the  $[M'(CN)_6]^{n-}$  vacancy content is low and the A-site cation content is high [5, 8]. Unfortunately, both of these features are a prerequisite for PBAs to be used as cathode materials [6]. However, the meta-study also indicated that the presence of water does not induce phase transitions, instead it modifies the magnitude of already existing distortions [8, 9]. The presence of water also influences other aspects of PBAs performance in a battery. For example, water's presence can hinder sodium-ion transport through the framework and modulate the voltage output for redox reactions of the transition metals [10, 11]. Thus, there is a complex interplay between the water content and electrochemical performance of PBAs.

To understand the various atomic and electronic structural influences, several robust structural models of hydrated and dehydrated PBAs need to be determined. Despite the large volume of research carried out on PBAs, the predominant use of x-ray diffraction (XRD) to study the structure has resulted in limited understanding of the mechanism behind the observed phase transitions [1, 8, 12]. Specifically for PW, there are inconsistencies regarding the structure of the hydrated phase. For example, Camacho *et al* reported a rhombohedral  $R\bar{3}$  structure for  $Na_{1.86}Fe[Fe(CN)_6] \cdot 1.92H_2O$  with oxygen positioned on half of the faces of the subcube [13]. This paper also reported a new orthorhombic Na-rich PBA ( $Na_{1.8}Fe[Fe(CN)_6] \cdot 0.7H_2O$ ) [13]. On the other hand, Rudola *et al* reported a monoclinic  $P2_1/n$  structure for  $Na_2Fe[Fe(CN)_6] \cdot 2H_2O$  with only a single oxygen atom at the face of the subcube [7]. Similarly, a monoclinic  $P2_1/n$  structure was determined for the compound  $Na_{1.88}Fe[Fe(CN)_6] \cdot 0.18H_2O$  but with oxygen randomly distributed on the six faces of the PBA subcube with  $Na^+$  ions in the center of the subcube [6]. Moreover, a rhombohedral  $R\bar{3}$  structure has been reported for  $Na_{1.76}Fe[Fe(CN)_6] \cdot 2.6H_2O$  with  $Na^+$  ions distributed over three different sites indicating  $Na^+$  disorder [14]. Later, the same group carried out another study on a similar compound  $Na_{1.76}Fe[Fe(CN)_6] \cdot 2.6H_2O$  and found a rhombohedral  $R\bar{3}$  structure with two oxygen sites randomly distributed over the six faces of the subcube and  $Na^+$  ions located in the center of the subcube [15]. Thus, there is not yet consensus in the literature regarding the structure and, in particular, the position of water in hydrated PW. In contrast, most studies agree upon the rhombohedral  $R\bar{3}$  structure for dry PW [6, 8, 13, 16].

These diffraction studies can also be compared to computational work on PBAs, which report that  $Na^+$  ions rather than water molecules occupy the faces of the subcubes due to the favorable electrostatic interaction between  $Na^+$  and the negatively charged  $N^-$  and the small size of  $Na^+$  [16–19]. Consequently, each  $Na^+$  ion is coordinated by two water molecules occupying the interstitial sites within the porous framework with the negative dipole of  $H_2O$  oriented towards the  $Na^+$  ion [17, 18]. The difference between computational and experimental structure as determined by XRD may originate from the similar scattering lengths of  $H_2O$  and  $Na^+$ , which both contain ten electrons. Thus, the structures should be reinvestigated utilizing neutron diffraction which can differentiate between both  $H_2O$  and  $Na^+$  as well as more accurately determine the positions of C and N compared to XRD.

There is a considerable lack of neutron diffraction studies of PBAs compared to x-rays [20–23]. One example is  $\text{Na}_{1.89}\text{Mn}[\text{Fe}(\text{CN})_6]_{0.97} \cdot 1.87 \text{H}_2\text{O}$ , which revealed  $P2_1/n$  symmetry with a single oxygen site at the face of each subcube [20]. Upon dehydration, the monoclinic structure transforms into a rhombohedral  $R\bar{3}$  structure with  $\text{Na}^+$  ions displacing along the  $c$  direction [20]. In other neutron studies of PBAs, the location of water within the structure has been included as high probability regions or clustering of oxygen atoms using computational methods [21, 22]. This indicates a disordered occupation of water in these materials. However, all neutron studies conclude that the space group symmetry, the water positions, and changes in site occupancies can be determined more accurately relative to previous x-rays studies. Thus, there is a need for neutron diffraction studies of PW, where none have been reported to date.

Here, we present the first neutron diffraction study of PW to determine accurate structures of the hydrated (H-PW) and dehydrated (D-PW) phases and follow the structural evolution between these phases from room temperature (RT,  $\sim 25^\circ\text{C}$ ) to  $250^\circ\text{C}$ . The observed phase transitions were modeled by symmetry-mode Rietveld refinements and differentiated from each other using the octahedral tilt descriptions previously reported [8]. The results revealed the role that water plays in determining and driving the phase transitions in PW. This provides a structural basis for explaining the electrochemical behavior and making rational design strategies when chemically modifying PW.

## 2. Experimental methods

### 2.1. Synthesis

Synthesis of each hydrated Prussian white (H-PW) batch proceeded by preparing a solution of 0.44 M  $\text{Na}_4[\text{Fe}(\text{CN})_6] \cdot 10\text{H}_2\text{O}$  (Sisco Research Laboratories Pvt. Ltd; extra pure AR, 99%) in deionised and deoxygenated water and heating to  $80^\circ\text{C}$ . An approximately two-fold molar excess of HCl (37%) was added over 12 h using a syringe pump to produce the acid-facilitated self-decomposition of  $\text{Na}_4[\text{Fe}(\text{CN})_6] \cdot 10\text{H}_2\text{O}$ .  $\text{N}_2$  was flowing during the reaction process that lasted 24 h. The obtained precipitate was filtered under inert conditions, washed four times with deionized and deoxygenated water, and finally dried under flowing  $\text{N}_2$  within the filtration setup for 12–24 h. Dehydrated Prussian White (D-PW) was prepared by drying a batch of H-PW at  $160^\circ\text{C}$  for 48 h under vacuum. The resulting powders were stored in an Ar glovebox for further studies.

Synthesis of PW via co-precipitation (CP-PW) proceeded by preparing two solutions in deoxygenated water stirring for 1 h. Solution A contained 0.1 M  $\text{FeSO}_4$ , 0.51 M sodium citrate, and 0.225 M ascorbic acid. Solution B contained 0.1 M  $\text{Na}_4\text{Fe}(\text{CN})_6$ . The two solutions were added to a reaction bottle containing deionized and deoxygenated water heated to  $80^\circ\text{C}$  at a constant rate of  $4 \text{ ml h}^{-1}$  over 13.5 h with stirring under flowing  $\text{N}_2$ . The reaction solution was further aged for 8 h before filtration, washing with deionized and deoxygenated water, and finally drying at ambient temperature for 24 h under inert conditions. The resulting powder was stored in an Ar glovebox for further studies.

### 2.2. Characterization

Sample composition was determined using inductively coupled plasma-optical emission spectroscopy (ICP-OES) to determine Na and Fe contents, while elemental analysis was used to determine C, N, H content. Measurements were performed by Medac Ltd, United Kingdom. Water content and dehydration temperature of the samples were studied with thermogravimetric analysis (TGA) using TA Instruments TGA Q500 by loading  $\sim 5 \text{ mg}$  of powder in an Al pan in air before placing the sample into the TGA furnace under flowing  $\text{N}_2$  ( $60 \text{ ml min}^{-1}$ ). The sample was heated to  $500^\circ\text{C}$  with a heating rate of  $5^\circ\text{C min}^{-1}$ . Particle size and morphology were investigated using scanning electron microscopy (SEM) on a SEM/EDS-Zeiss 1550 instrument working with an acceleration voltage of 3 kV using an in-lens detector. The sample was loaded onto carbon tape in a glovebox and quickly transferred into the vacuum chamber of the microscope.

Mössbauer measurements were carried out at RT using constant acceleration type of vibrator and a  $^{57}\text{CoRh}$  source. The samples were enclosed in a sealed Al cover. The so-formed absorber had a sample concentration of  $\sim 10 \text{ mg cm}^{-2}$ . Calibration spectra were recorded at 295 K using natural Fe metal foil as a reference absorber. The spectra were folded and fitted using the least square Mössbauer fitting program Recoil to obtain the values of the center shift CS, the magnitude of the electric quadrupole splitting IQSI, the full-width at half maxima  $W$  of the Lorentzian absorption lines, and the spectral areas  $A$ .

Samples were prepared for laboratory XRD experiments by dispersing the powder on a single crystal Si disc. Powder XRD measurements were performed on a Bruker D8 TwinTwin diffractometer (double  $\text{Cu K}\alpha$  radiation  $\lambda_1 = 1.540600 \text{ \AA}$ ,  $\lambda_2 = 1.544390 \text{ \AA}$ ) with a Lynx-eye XE-T position sensitive detector. The experiments were conducted between  $10$  and  $80^\circ$  in steps of  $0.02^\circ$ . Synchrotron powder XRD data were collected on the high-resolution powder diffraction beamline P02.1 at PETRA III, Hamburg, Germany [24]. The wavelength was determined to be  $0.20734 \text{ \AA}$  from measurements of a  $\text{LaB}_6$  standard (NIST660c).

The samples were filled into 0.3 mm glass capillaries in an argon-filled glovebox for high temperature measurements using a capillary spinner and Oxford hot-air blower with a variable heating rate. The diffraction patterns were collected using a Varex XRD 4343CT detector ( $150 \times 150 \mu\text{m}^2$  pixel size,  $2880 \times 2880$  pixel area). The obtained 2D patterns were integrated into 1D diffraction patterns using Dawn [25]. Neutron powder diffraction (ND) data were collected on the time-of-flight instrument POLARIS [26] at the ISIS Pulsed Neutron and Muon Source [27]. 1.6960 g of H-PW was loaded into an open cylindrical vanadium can and measured continuously from RT to 250 °C with a heating rate of  $0.4 \text{ }^\circ\text{C min}^{-1}$  with a 1 h collection time at RT, 1 h and 50 min collection time at 250 °C and a collection time of 10 min for each of the patterns during heating. Upon cooling, diffraction data was measured with a collection time of 4 min/pattern with a cooling rate of  $\sim 1.25 \text{ }^\circ\text{C min}^{-1}$ . 1.6095 g of D-PW was loaded into an open cylindrical vanadium can, cooled to 4 K, and measured for 12 h at 4 K. All refinements were performed using the Rietveld method [28] with symmetry-mode refinements using ISODISTORT [29] in the TOPAS software [30] where scale factors, cell parameters, peak shape, and atomic displacement factors (ADPs) were refined.

### 3. Results and discussion

#### 3.1. Composition and initial characterization

ICP-OES analysis of H-PW revealed the composition  $\text{Na}_{2.14(7)}\text{Fe}[\text{Fe}(\text{CN})_6] \cdot z\text{H}_2\text{O}$  indicating a successful synthesis of Na-rich, low vacancy PW (table S1). TGA measurement of H-PW (figure S1) shows a weight loss of  $\sim 10.54(3)$  wt% when  $T < 225 \text{ }^\circ\text{C}$ , which corresponds to the release of surface adsorbed water and interstitial water ( $= 2.07(2)$   $\text{H}_2\text{O}$  per formula unit (f.u.)). Similarly, the composition of the PW sample synthesized by co-precipitation (CP-PW) was determined to be  $\text{Na}_{2.17(5)}\text{Fe}[\text{Fe}(\text{CN})_6] \cdot 1.96(2)\text{H}_2\text{O}$  from ICP-OES and TGA analysis (figure S1, table S1) and the composition of D-PW was determined to be  $\text{Na}_{2.08(7)}\text{Fe}[\text{Fe}(\text{CN})_6]_{0.98(2)}$  (table S1).

All samples have similar cubic morphology with H-PW and D-PW being micron-sized particles (as previously reported [6]) and CP-PW being multifaceted intergrown micron-sized particles (figure S2).

The Mössbauer spectrum at 295 K of H-PW (figure S3) shows a three-line structure, which was fitted using two quadrupole split doublets. The central unresolved line originates from low spin  $\text{Fe}^{2+}_{\text{C}}$  and the well-resolved doublet originates from high spin  $\text{Fe}^{2+}_{\text{N}}$ . The fitting parameters are presented in table S2. The hyperfine parameters are in good agreement with the results from earlier studies of PW [5, 6, 31]. The nominal value of Fe vacancies at the low spin site was verified from the Mössbauer spectral areas corresponding to low spin  $\text{Fe}_{\text{C}}$  and the high spin  $\text{Fe}_{\text{N}}$ . The areas were 47(3):53(3) indicating a vacancy-free structure.

Laboratory XRD was performed immediately following the synthesis of H-PW and revealed that the material adopts a monoclinic structure with space group  $P2_1/n$  (figure S4).

#### 3.2. Near room temperature octahedral tilt transition in PW

Neutron powder diffraction data were collected from RT up to 250 °C from H-PW. In the RT pattern, two phases were observed due to an incomplete phase transition which occurs between 30 to 40 °C from  $P2_1/n$  to  $R\bar{3}$ . The presence of the  $R\bar{3}$  phase can be seen in figure 2 by the appearance of the  $20\bar{4}$  reflection between the 022 and 400 reflections of the  $P2_1/n$  phase in the peak at 2.6 Å. A small amount of intensity of the  $P2_1/n$  reflections was observed at 33 °C with all the intensity gone by 40 °C. Thus, the transition is likely complete at  $\sim 35 \text{ }^\circ\text{C}$ . This phase transition was also observed for a sample with similar composition  $\text{Na}_{2.17(5)}\text{Fe}[\text{Fe}(\text{CN})_6] \cdot 1.96(2)\text{H}_2\text{O}$ , CP-PW, prepared by co-precipitation. From synchrotron XRD (figures S5 and S6), CP-PW undergoes the same phase transition from  $P2_1/n$  to  $R\bar{3}$  between 30 to 40 °C. Hence, the phase transition near RT for Na-rich PW is independent of the synthesis method. The existence of both structures for the same compound near to RT has not been reported previously, although the two structures have been reported independently at RT [7, 13, 15].

The difference between the  $P2_1/n$  and  $R\bar{3}$  structures relates to octahedral tilting [32]. Octahedral tilting involves either in-phase or out-of-phase rotation of the transition metal octahedra in PBAs. This is described by Glazer notation with '+' for in-phase and '-' for out-of-phase tilts with the lowercase letter denoting the relative magnitude of the tilt [32]. For PBAs with a high sodium or potassium content, the most prevalent tilt pattern is  $a^- a^- b^+$ , which drives the monoclinic  $P2_1/n$  symmetry. This involves an in-phase tilt of the octahedra around one of the pseudo-cubic unit cell axes with out-of-phase tilts along the other two directions [33]. A tilt pattern of  $a^- a^- a^-$  gives rise to rhombohedral  $R\bar{3}$  symmetry, which is often seen for dehydrated sodium-containing PBAs. In this case, the tilting is out-of-phase for all three pseudo-cubic unit cell axes. It is the single in-phase tilt which gives rise to the split peaks in figure 2, which indicates that one of the crystallographic axes differs from the other two ( $P2_1/n$ ).

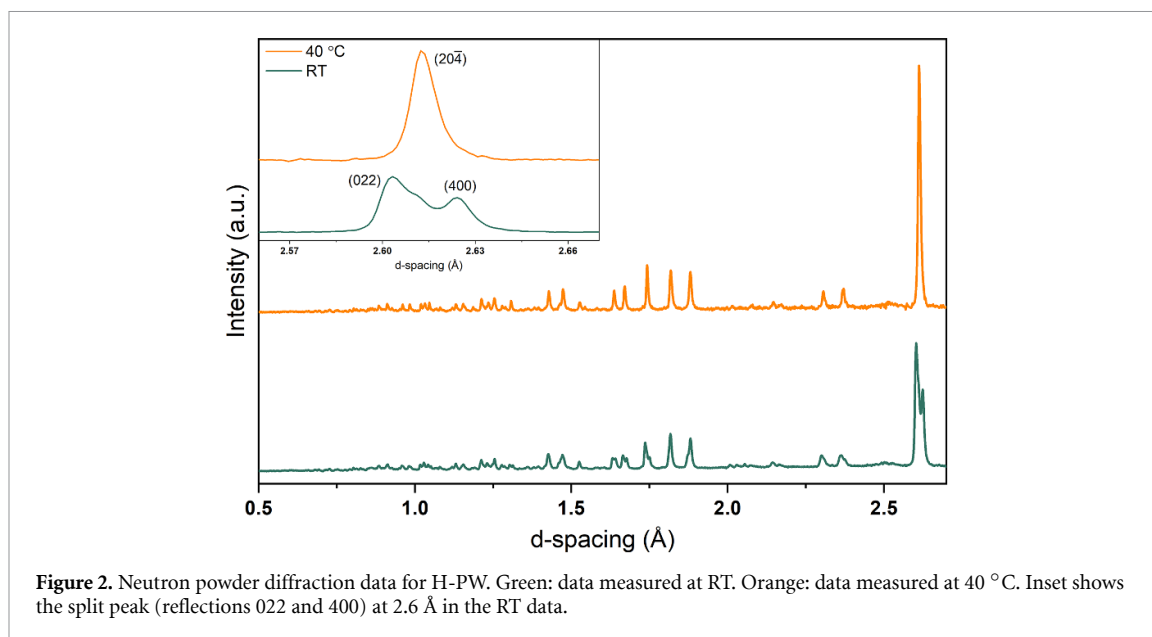


**Figure 2.** Neutron powder diffraction data for H-PW. Green: data measured at RT. Orange: data measured at 40 °C. Inset shows the split peak (reflections 022 and 400) at 2.6 Å in the RT data.

### 3.2.1. Refinements of the two near room temperature phases

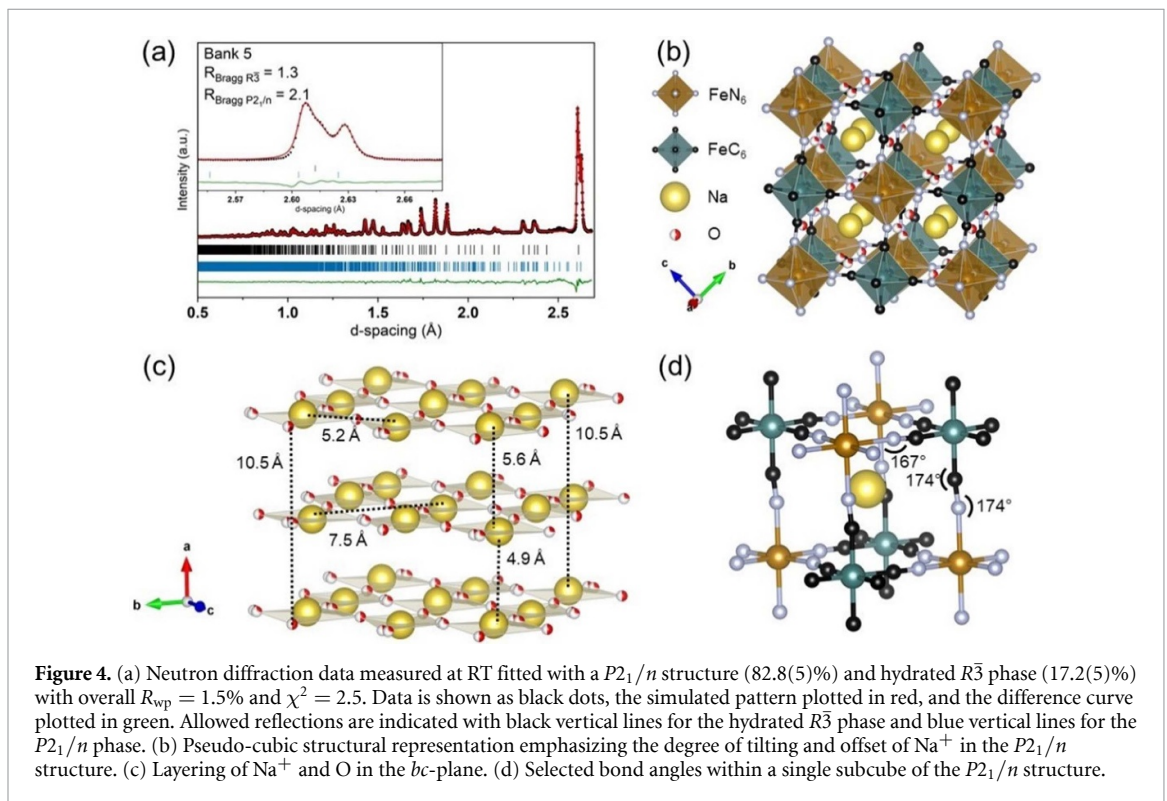
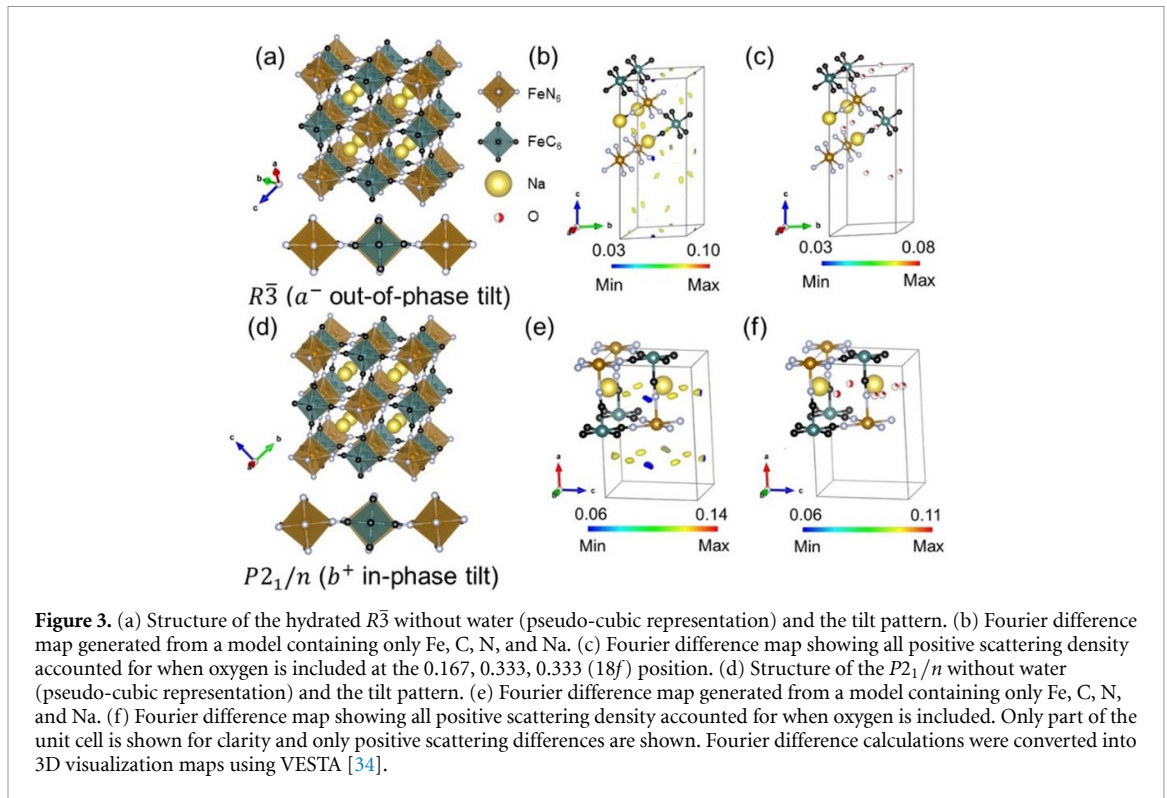
Since the phase transition occurs close to RT, it is difficult to refine the pure  $P2_1/n$  phase due to the presence of a second  $R\bar{3}$  phase, which complicates the modeling of the neutron diffraction data. The  $R\bar{3}$  phase was refined against data collected at 40 °C since the phase transition is complete at this temperature.

The PBA framework model with sodium included was refined prior to calculating Fourier difference maps to locate the water molecules within the structure. A  $R\bar{3}$  model containing Fe, C, N, and Na was fitted to the 40 °C data. The refined framework structure is shown in figure 3(a) including the out-of-phase tilt along the  $a$  direction of the pseudo-cubic unit cell. Water positions from the literature were tested to see if the scattering difference observed in the Fourier difference maps (figure 3(b)) was accounted for. The  $R\bar{3}$  model from Wang *et al* [14] was applied by replacing two of the lower occupancy  $\text{Na}^+$  ions with oxygen atoms (located at  $-0.167, 0.167, 0.167$  and  $0.167, 0.333, 0.333$  (Wyckoff position  $18f$ )). This yielded a reasonable fit with all positive scattering difference accounted for (figure 3(c)), although with high ADPs for the oxygen atoms. Refinement of the oxygen occupancies resulted in zero occupancy of the oxygen site located at  $-0.167, 0.167, 0.167$  ( $18f$ ), which was subsequently removed from the model. This gave a stable refinement with reasonable ADPs for the oxygen site located at  $0.167, 0.333, 0.333$  ( $18f$ ). Hydrogen atoms were not refined due to the positional and orientation disorder of the water molecules. Inclusion of hydrogen barely changes the simulated neutron diffraction pattern and subsequently does not affect the quality of the fit (figure S7). Similar results are reported in previous studies [20, 22, 23].

The established  $R\bar{3}$  model from the 40 °C data was fixed as the second phase in the RT data. The host framework structure of the primary  $P2_1/n$  phase containing Fe, C, N, and Na was refined from a starting model reported by Song *et al* [20] and is presented in figure 3(d) including the in-phase tilt along the  $a$  direction of the parent cubic unit cell. Similar to the  $R\bar{3}$  model, Fourier difference maps were generated to determine the position of oxygen atoms. This revealed two possible sites (figure 3(e)), which were compared to sites reported in a previous  $P2_1/n$  model [6]. Inclusion of two oxygen sites on the  $4e$  Wyckoff position within the  $bc$ -plane removed all the positive scattering differences (figure 3(f)), though the ADPs of the oxygen atoms were high. A closer inspection of the Fourier difference maps revealed an elongation of the observed positive scattering differences. Hence, one of the oxygen atoms was split into two sites, which reduced the ADPs and improved the stability of the refinement. The hydrogen positions were not refined for reasons outlined above.

The final refined models with oxygen included are displayed in figures 4(a), (b) and S8, S9 with refinement details in tables S3 and S4. The model fitted to the RT data consists mainly of the  $P2_1/n$  structure (82.8(5) %) with a minor hydrated  $R\bar{3}$  phase (17.2(5) %). The data measured at 40 °C is fitted with a single hydrated  $R\bar{3}$  structure.

In the RT  $P2_1/n$  structure,  $\text{Na}^+$  is coordinated to a random distribution of O atoms within the  $bc$ -plane resulting in only four faces of each subcube occupied by O (figure 4(c)). This results in clear  $\text{Na}^+$  channels along  $a$ . Interestingly, the in-phase tilt  $b^+$  also lies along the  $a$  direction implying that the positioning of water might direct the nature of tilting in PBAs. Layering of  $\text{Na}^+$  and O in the  $bc$ -plane was also found for the  $P2_1/n$  structure of  $\text{Na}_{1.89}\text{Mn}[\text{Fe}(\text{CN})_6]_{0.97} \cdot 1.87\text{H}_2\text{O}$  [20]. For the  $P2_1/n$  model in the present study, one



of the O atoms was included as a split site. This can be explained by considering the ideal Na–O bond distance for water coordinated to  $\text{Na}^+$  ions, which is 2.3 Å [7, 20]. The distance between the center of mass for the split site and a neighboring  $\text{Na}^+$  is 2.6 Å. Thus, in reality water must lie slightly closer to one of the two  $\text{Na}^+$  ions. These displacements are not long-range ordered leading to the appearance of a split site on average. The obtained bond angles for the  $P2_1/n$  structure reported here agree with those previously reported [6, 14] with the Fe–N–C bond angle being similar to or less than the Fe–C–N bond angles. This is due to the  $\sigma$ -bonding character of the Fe–N bond providing higher flexibility (figure 4(d)) [18, 20].

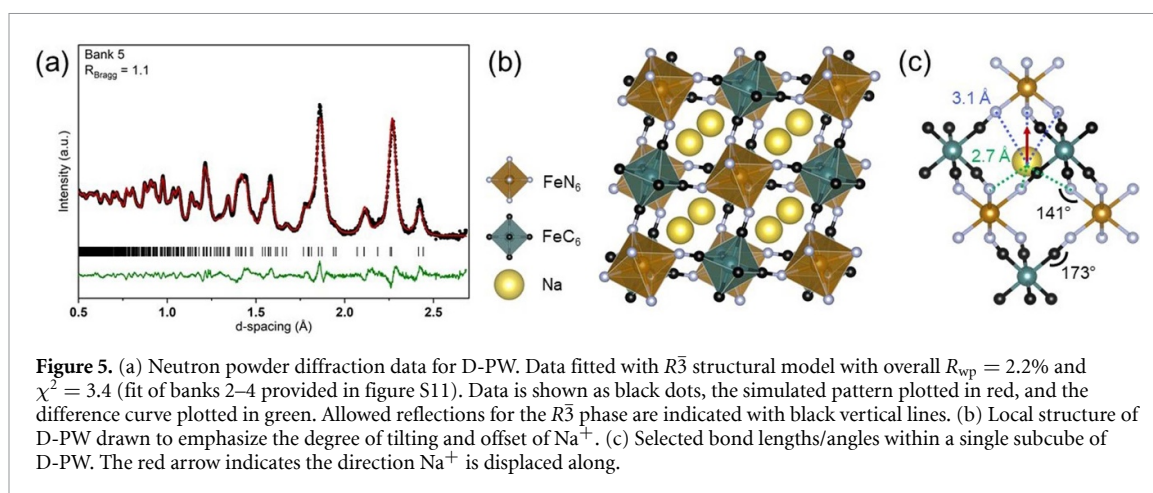


**Figure 5.** (a) Neutron powder diffraction data for D-PW. Data fitted with  $R\bar{3}$  structural model with overall  $R_{wp} = 2.2\%$  and  $\chi^2 = 3.4$  (fit of banks 2–4 provided in figure S11). Data is shown as black dots, the simulated pattern plotted in red, and the difference curve plotted in green. Allowed reflections for the  $R\bar{3}$  phase are indicated with black vertical lines. (b) Local structure of D-PW drawn to emphasize the degree of tilting and offset of  $\text{Na}^+$ . (c) Selected bond lengths/angles within a single subcube of D-PW. The red arrow indicates the direction  $\text{Na}^+$  is displaced along.

**Table 1.** Selected rotation angles and bond distances in H-PW and D-PW ( $R\bar{3}$ ).

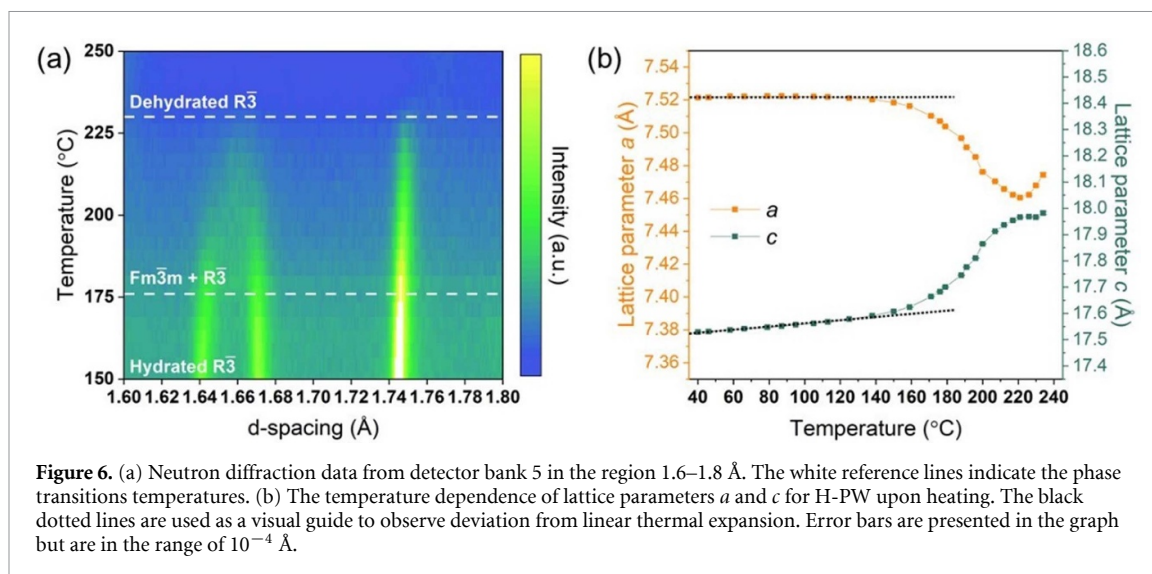
Rotation angles/bond distances	H-PW	D-PW	Difference
$\text{Fe}_N\text{-Fe}_C\text{-C}$	$1.52(7)^\circ$	$18.96(4)^\circ$	$17.44(6)^\circ$
$\text{Fe}_C\text{-Fe}_N\text{-N}$	$1.69(1)^\circ$	$24.29(4)^\circ$	$22.60(4)^\circ$
$\text{Fe}_C\text{-Na}$	$4.421(3) \text{ \AA}$	$5.773(4) \text{ \AA}$	$1.352(3) \text{ \AA}$
$\text{Fe}_N\text{-Na}$	$4.344(3) \text{ \AA}$	$3.722(4) \text{ \AA}$	$-0.622(3) \text{ \AA}$

Transitioning to the hydrated  $R\bar{3}$  structure determined at  $40^\circ\text{C}$  (figure S9), O instead appears to be randomly distributed over three faces of each subcube. Here, there are no clear  $\text{Na}^+$  channels in any direction. It should be noted, however, that several distributions of the O atoms were tested which resulted in similar ADPs and quality of fits. This can partly be explained by the short collection time (10 min) of the  $40^\circ\text{C}$  data. All models provided equal quality of fits except for one model containing O atoms on both the  $-0.167, 0.167, 0.167$  and  $0.167, 0.333, 0.333$  sites, which did not calculate any intensity for the 003 reflection in the bank 2 data. Thus, it is difficult to draw any compelling conclusions about the arrangement of water in the  $R\bar{3}$  phase, except for the higher degree of disorder compared to the  $P2_1/n$  structure. Aside from the change in the tilting system between the  $P2_1/n$  and  $R\bar{3}$  structures (figure 3) and very minor change of the offset of  $\text{Na}^+$  within a subcube (figure S10), all bond distances and angles remain similar. Insight into the local structure using total scattering techniques would unravel any local order of water in the hydrated  $R\bar{3}$  structure. In summary, the  $P2_1/n$  and  $R\bar{3}$  structures can both exist for a single compound and the structures were determined with higher degree of confidence due to the use of neutron diffraction.

### 3.3. Dehydration of PW

Prior to use in SIBs, PW is dehydrated which results in structural collapse. To investigate the distortions driving this change in detail, neutron diffraction data were collected on a fully dehydrated sample, D-PW. These data were initially modeled using the obtained hydrated  $R\bar{3}$  model without the O atoms included (figures 5(a) and (b), tables S5 and S6). The structure agrees with previously reported structures of dehydrated PW from x-ray data and *ab initio* calculations [6, 16]. Upon dehydration, the volume reduces by 20% relative to the hydrated material, leading to loss of crystallinity (as indicated by peak broadening) in line with previous studies [6, 20]. Symmetry-mode refinement allows the causes of this phase transition to be understood more clearly. The key distortion modes identified were displacement of  $\text{Na}^+$  along  $c$  towards the  $\text{FeN}_6$  octahedra and the tilting of rigid  $\text{FeN}_6$  and  $\text{FeC}_6$  octahedra. As expected, due to the  $\pi$ -bonding character of the Fe–C bond, the Fe–C–N bond angle does not deviate significantly from the hydrated material (figure 5(c)) [18, 20]. Finally, Fe–C/N bond distances remain unchanged relative to the hydrated material.

Summarizing the observed changes, the mechanism for the volume collapse can be described. The  $\text{Na}^+$  ions displace along the  $c$  direction due to Coulombic attraction to the higher electron density on the N-bound Fe atom. The N atoms opposite are pulled with the  $\text{Na}^+$  ion towards the same direction of displacement due to the same Coulombic attraction resulting in short Na–N distances. At the same time, the rigid octahedra are rotated. The structural collapse is also evident looking at the rotation of the octahedra (table 1). In the hydrated  $R\bar{3}$  structure of H-PW, the  $\text{FeC}_6$  octahedra are rotated  $1.69(1)^\circ$  while the  $\text{FeN}_6$  octahedra are rotated  $1.52(7)^\circ$ . Upon dehydration, the  $\text{FeC}_6$  octahedra rotate  $17.44(6)^\circ$  while the  $\text{FeN}_6$  octahedra rotate  $22.60(4)^\circ$ , thus, the magnitude of the tilt in the  $a^-a^-a^-$  tilt pattern increases. It is



reasonable that the  $\text{FeN}_6$  octahedra rotate to a larger degree due to the Coulomb attraction between  $\text{Na}^+$  and  $\text{N}^-$  and the stronger Fe–C bond providing less flexibility [11, 18, 35]. Finally, the removal of water does not change the nature of distortions in PBAs, but rather modifies the magnitude of the pre-existing distortions.

### 3.4. Variable temperature studies of PW

To study the dehydration mechanism, the structural evolution of H-PW was followed during heating using x-ray and neutron diffraction (figures 6(a) and S12). Initially, PW adopts a  $P2_1/n$  structure which converts to a hydrated  $R\bar{3}$  structure close to 35 °C. From the synchrotron XRD data, H-PW transforms from the hydrated  $R\bar{3}$  phase to a cubic  $Fm\bar{3}m$  phase at  $\sim 120$  °C as evidenced by the appearance of the 440 cubic reflection between the  $4\bar{2}0$  and 208 reflections of the hydrated  $R\bar{3}$ . This cubic phase coexists with the dehydrated  $R\bar{3}$  phase from 220 °C to 245 °C when heated at a rate of 1 °C  $\text{min}^{-1}$  (figure S12). Interestingly, the transition to  $Fm\bar{3}m$  begins at 176 °C in the ND data (figure 6(a)) and the transition to cubic did not go to completion before complete conversion to the dehydrated  $R\bar{3}$  phase at 230 °C. Here, a heating rate of 0.4 °C  $\text{min}^{-1}$  was applied. In this case, the ND experiment used a larger sample volume compared to the XRD experiment ( $\sim 2$  g vs  $\sim 2$  mg) potentially leading to lower heating efficiency through the whole sample. Previous work on  $\text{Na}_{1.76}\text{Fe}[\text{Fe}(\text{CN})_6] \cdot 2.6\text{H}_2\text{O}$  revealed that the cubic  $Fm\bar{3}m$  phase appears at 150 °C when heated at 3 °C  $\text{min}^{-1}$  and continues to coexist with a high-temperature  $R\bar{3}$  phase until 300 °C [15].

It is clear that the dehydration process is kinetically limited and thus dependent on the heating efficiency and heating rate. The sluggish kinetics of dehydration is likely due to a combination of strong bonding of water to sodium within the structure [31], large diffusion distances through the micron-sized particles, and the energy cost associated with induced strain from the phase transition to the dehydrated  $R\bar{3}$  structure. It has been previously shown that  $\text{Na}^+$  ion diffusion through the structure is similarly affected by the presence of water [10]. Further insight on the impact of water and the temperature at which it begins to leave the structure can be obtained from the cell parameter changes during the variable temperature experiment (figure 6(c)).

The thermal expansion of H-PW was extracted from the variable temperature data in the range 40–140 °C. The thermal expansion coefficients were calculated using PASCAL [36]. In contrast to most PBAs [37, 38], H-PW exhibits anisotropic thermal expansion and a small positive volumetric expansion upon heating. The coefficients of thermal expansion (CTE) are  $\alpha_{ab} = -1.2(9) \text{ MK}^{-1}$  for the  $ab$ -plane and  $\alpha_c = 34(2) \text{ MK}^{-1}$  for the  $c$  direction. After dehydration, the sample (now called DH-PW) was cooled from 250 °C down to 35 °C. DH-PW also shows anisotropic thermal expansion with the  $ab$ -plane expanding and the  $c$  direction contracting with corresponding CTEs of  $\alpha_{ab} = 52.2(3) \text{ MK}^{-1}$  and  $\alpha_c = -31.1(2) \text{ MK}^{-1}$  over the temperature range measured. DH-PW also exhibits positive volumetric expansion with a higher rate compared to the hydrated phase. Most PBAs show isotropic negative thermal expansion upon heating (due to their cubic symmetry) with very low magnitudes of CTE [37–40]. The different behavior of PW is a result of the lower symmetry, however, the lack of thermal expansion studies of other distorted PBAs prevents more in-depth comparison. However, the difference between H-PW and DH-PW indicates that the presence of water has a strong influence on the sign and magnitude of the expansion.

## 4. Conclusions

As the presence of water has a significant effect on the material performance of PW ( $\text{Na}_2\text{Fe}[\text{Fe}(\text{CN})_6] \cdot z\text{H}_2\text{O}$ ), a solid structural understanding is needed to rationalize the electrochemical properties and improve the material. This was achieved in this study using neutron diffraction. For the first time it was shown that both a monoclinic and hydrated rhombohedral structure for a single composition of PW exist near RT independently of the synthesis method. During this phase transition, the ordering of the water is lost and this ordering transition is accompanied to a change in the nature of the octahedral tilting distortions. This observation subsequently proved the previous hypothesis that water does not induce phase transitions, but rather modifies the magnitude of pre-existing distortions as the symmetry of the structure was maintained during dehydration. Therefore, the phase transition is an inherent property of cation rich PBAs and replacement of water with another small neutral molecule is a viable strategy to modifying the magnitude of volume change. Finally, the onset of dehydration occurs earlier, around 120 °C, than previously reported [15]. However, the removal of water is kinetically hindered and subsequent phase transitions, such as the appearance of the metastable cubic PW, are heavily dependent on the measurement conditions. This work provides vital insight into how water content influences phase transitions and tilting in PW. The structural models determined here will be useful for modeling of diffusion pathways as well as understanding and predicting how neutral guest species influence structural stability and electronic structure in PBAs.

## Data availability statement

The data that support the findings of this study are openly available at the following URL/DOI: <https://doi.org/10.5286/ISIS.E.RB2010290-1>.

## Acknowledgments

This research is funded by Stiftelsen för Strategisk Forskning (SSF) within the Swedish National Graduate School in Neutron Scattering, SwedNess (GSn15–0008). The authors also gratefully acknowledge funding from the Strategic Research Area StandUp for Energy and Energimyndigheten (45517-1). We acknowledge DESY (Hamburg, Germany), a member of the Helmholtz Association HGF, for the provision of experimental facilities. Parts of this research were carried out at PETRA III using beamline P02.1 and we would like to thank Alexander Schökel and Volodymyr Baran for assistance. We acknowledge the Science and Technology Facilities Council (STFC) for access to neutron beamtime at ISIS and also for the provision of sample preparation at the POLARIS instrument.

## Conflict of interest

W R B is a co-founder of the company ALTRIS AB which produces Prussian white powder for sodium-ion battery applications.

## ORCID iDs

Ida Nielsen  <https://orcid.org/0000-0002-6511-8291>

D O Ojwang  <https://orcid.org/0000-0001-9304-8975>

P F Henry  <https://orcid.org/0000-0003-4714-6587>

G Ek  <https://orcid.org/0000-0003-4831-3842>

H L B Boström  <https://orcid.org/0000-0002-8804-298X>

W R Brant  <https://orcid.org/0000-0002-8658-8938>

## References

- [1] Ivanov V D 2020 Four decades of electrochemical investigation of Prussian blue *Ionic* **26** 531–47
- [2] Liu Q *et al* 2020 The cathode choice for commercialization of sodium-ion batteries: layered transition metal oxides versus Prussian blue analogs *Adv. Funct. Mater.* **30** 1909530
- [3] Bauer A *et al* 2018 The scale-up and commercialization of nonaqueous Na-ion battery technologies *Adv. Energy Mater.* **8** 1–13
- [4] Wang L *et al* 2015 Rhombohedral Prussian white as cathode for rechargeable sodium-ion batteries *J. Am. Chem. Soc.* **137** 2548–54
- [5] Ojwang D O *et al* 2021 Moisture-driven degradation pathways in Prussian white cathode material for sodium-ion batteries *ACS Appl. Mater. Interfaces* **13** 10054–63
- [6] Brant W R *et al* 2019 Selective control of composition in Prussian white for enhanced material properties *Chem. Mater.* **31** 7203–11

- [7] Rudola A *et al* 2017 Monoclinic sodium iron hexacyanoferrate cathode and non-flammable glyme-based electrolyte for inexpensive sodium-ion batteries *J. Electrochem. Soc.* **164** A1098–109
- [8] Boström H L B *et al* 2022 Octahedral tilting in Prussian blue analogues *J. Mater. Chem. C* **10** 1–24
- [9] Tapia-Ruiz N *et al* 2021 2021 roadmap for sodium-ion batteries *J. Phys. Energy* **3** 031503
- [10] Ojwang D O *et al* 2022 Guest water hinders sodium-ion diffusion in low-defect Berlin green cathode material *Dalton Trans.* **51** 14712–20
- [11] Guo X *et al* 2019 Water contributes to higher energy density and cycling stability of Prussian blue analogue cathodes for aqueous sodium-ion batteries *Chem. Mater.* **31** 5933–42
- [12] Boström H L B *et al* 2019 Structure and thermal expansion of the distorted Prussian blue analogue RbCuCo(CN)<sub>6</sub> *Chem. Commun.* **55** 10230–3
- [13] Camacho P S *et al* 2021 Impact of synthesis conditions in Na-Rich Prussian blue analogues *ACS Appl. Mater. Interfaces* **13** 42682–92
- [14] Wang W *et al* 2020 Understanding rhombohedral iron hexacyanoferrate with three different sodium positions for high power and long stability sodium-ion battery *Energy Storage Mater.* **30** 42–51
- [15] Wang W *et al* 2022 Effect of eliminating water in Prussian blue cathode for sodium-ion batteries *Adv. Funct. Mater.* **32** 2111727
- [16] Wang Y P *et al* 2022 Structural evolution, redox mechanism, and ionic diffusion in rhombohedral Na<sub>2</sub>FeFe(CN)<sub>6</sub> for sodium-ion batteries: first-principles calculations *J. Electrochem. Soc.* **169** 010525
- [17] Liu S *et al* 2022 Effects of interstitial water and alkali cations on the expansion, intercalation potential, and orbital coupling of nickel hexacyanoferrate from first principles *J. Appl. Phys.* **131** 105101
- [18] Xiao P *et al* 2015 Theoretical study of the structural evolution of a Na<sub>2</sub>FeMn(CN)<sub>6</sub> cathode upon Na intercalation *Chem. Mater.* **27** 3763–8
- [19] Ling C *et al* 2013 First-principles study of alkali and alkaline earth ion intercalation in iron hexacyanoferrate: the important role of ionic radius *J. Phys. Chem. C* **117** 21158–65
- [20] Song J *et al* 2015 Removal of interstitial H<sub>2</sub>O in hexacyanometallates for a superior cathode of a sodium-ion battery *J. Am. Chem. Soc.* **137** 2658–64
- [21] Morozova P A *et al* 2021 Exploring the role of crystal water in potassium manganese hexacyanoferrate as a cathode material for potassium-ion batteries *Crystals* **11** 895
- [22] Bhatt P *et al* 2013 Evidence for the existence of oxygen clustering and understanding of structural disorder in Prussian blue analogues molecular magnet M<sub>1.5</sub>[Cr(CN)<sub>6</sub>]<sub>2</sub>·zH<sub>2</sub>O (M = Fe and Co): reverse Monte Carlo simulation and neutron diffraction study *J. Phys. Chem. C* **117** 2676–87
- [23] Wardecki D *et al* 2017 Neutron diffraction and EXAFS studies of K<sub>2x/3</sub>Cu[Fe(CN)<sub>6</sub>]<sub>2/3</sub>·nH<sub>2</sub>O *Cryst. Growth Des.* **17** 1285–92
- [24] Dippel A-C *et al* 2015 Beamline P02.1 at PETRA III for high-resolution and high-energy powder diffraction *J. Synchrotron Radiat.* **22** 675–87
- [25] Filik J *et al* 2017 Processing two-dimensional x-ray diffraction and small-angle scattering data in DAWN 2 *J. Appl. Crystallogr.* **50** 959–66
- [26] Smith R I *et al* 2019 The upgraded Polaris powder diffractometer at the ISIS neutron source *Rev. Sci. Instrum.* **90** 115101
- [27] W Brant *et al* 2021 Link between thermal behaviour, positions of structural water and sodium content in low vacancy Prussian white *STFC ISIS Neutron and Muon Source* (<https://doi.org/10.5286/ISIS.E.RB2010290-1>)
- [28] Rietveld H M 1969 A profile refinement method for nuclear and magnetic structures *J. Appl. Crystallogr.* **2** 65–71
- [29] Campbell B J *et al* 2006 ISODISPLACE: a web-based tool for exploring structural distortions *J. Appl. Crystallogr.* **39** 607–14
- [30] Coelho A A 2018 TOPAS and TOPAS-academic: an optimization program integrating computer algebra and crystallographic objects written in C++: an *J. Appl. Crystallogr.* **51** 210–8
- [31] Ojwang D O *et al* 2020 Influence of sodium content on the thermal behavior of low vacancy Prussian white cathode material *Dalton Trans.* **49** 3570–9
- [32] Glazer A M 1972 The classification of tilted octahedra in perovskites *Acta Crystallogr. B* **28** 3384–92
- [33] Howard C J *et al* 2003 Ordered double perovskites—a group-theoretical analysis *Acta Crystallogr. B* **59** 463–71
- [34] Momma K *et al* 2011 VESTA 3 for three-dimensional visualization of crystal, volumetric and morphology data *J. Appl. Crystallogr.* **44** 1272–6
- [35] Zhou A *et al* 2021 Hexacyanoferrate-type Prussian blue analogs: principles and advances toward high-performance sodium and potassium ion batteries *Adv. Energy Mater.* **11** 1–35
- [36] Cliffe M J *et al* 2012 PASCAL: a principal axis strain calculator for thermal expansion and compressibility determination *J. Appl. Crystallogr.* **45** 1321–9
- [37] Chapman K W *et al* 2006 Compositional dependence of negative thermal expansion in the Prussian blue analogues M<sup>II</sup>Pt<sup>IV</sup>(CN)<sub>6</sub> (M = Mn, Fe, Co, Ni, Cu, Zn, Cd) *J. Am. Chem. Soc.* **128** 7009–14
- [38] Shi N *et al* 2019 Negative thermal expansion in cubic FeFe(CN)<sub>6</sub> Prussian blue analogues *Dalton Trans.* **48** 3658–63
- [39] Adak S *et al* 2011 Thermal expansion in 3d-metal Prussian blue analogs—a survey study *J. Solid State Chem.* **184** 2854–61
- [40] Gao Q *et al* 2018 Tunable thermal expansion from negative, zero, to positive in cubic Prussian blue analogues of GaFe(CN)<sub>6</sub> *Inorg. Chem.* **57** 14027–30